The Astronomical Journal, 166:215 (7pp), 2023 November https://doi.org/10.3847/1538-3881/ad004a

KIC 9028474: A Long-period Eclipsing Binary on a Highly Eccentric Orbit

Orkun Özdarcan
Department of Astronomy and Space Sciences, Faculty of Science, Ege University, 35100 İzmir, Turkey; orkun.ozdarcan@ege.edu.tr
Received 2023 August 1; revised 2023 September 23; accepted 2023 September 25; published 2023 October 30

Abstract

We present a comprehensive analysis of a very long-period (124.93669 days) eclipsing binary KIC 9028474, which is composed of F9V+G1V components on a highly eccentric ($e = 0.82029$) orbit. Masses and radii of the primary and the secondary components are $M_1 = 1.18 \pm 0.04\,M_\odot$, $M_2 = 1.04 \pm 0.03\,M_\odot$, $R_1 = 1.52 \pm 0.02\,R_\odot$, and $R_2 = 1.11 \pm 0.01\,R_\odot$, respectively. Eclipse time variations show the presence of apsidal motion, which in turn shows the existence of a third body in a relatively close orbit. Simultaneous analysis of infrared spectra and space photometry reveals that the primary component is about to leave the main sequence, indicating an age of 5.2 ± 0.8 Gyr for the system. Theoretical evaluation of the observed eccentricity indicates that the components of KIC 9028474 will end their whole life much before the orbital circularization is achieved. Given the limited resolution of the spectra, we can only place an upper limit on the rotational velocities of each star, thus a theoretical evaluation of the synchronization of the components.

Unified Astronomy Thesaurus concepts: Eclipsing binary stars (444); Detached binary stars (375); Fundamental parameters of stars (555); Eccentricity (441)

1. Introduction

Close binary systems with eccentric orbits are the objects of interest in researches those focus on the tidal interaction and the dissipation effects, which reduce the eccentricity of the orbit in time and finally lead to a circular orbit for these systems. Roles of dynamical and equilibrium tides were studied by Zahn (1975, 1977), while Tassoul (1987, 1988) investigated the problem together with the orbital synchronization process in hydrodynamical aspects. Observational tests of these studies require precisely determined fundamental parameters (i.e., mass and radius) of stars. At that point, double-lined detached eclipsing binaries (SB2-DEB) come forward because precise mass and radius determination is possible for the components of SB2-DEB systems (Andersen 1991).

Sky surveys and space telescopes provide enormous amounts of spectroscopic and photometric data for stellar astrophysics. Inspection of this huge data stack leads to the discovery of rare interesting systems. KIC 9028474 is such an object, which is an eclipsing binary system with a long orbital period and a very high eccentricity. Our target system was first classified as an eclipsing binary in Kepler Eclipsing Binary Catalogue[1] (Prša et al. 2011; Slawson et al. 2011). After a while, Dong et al. (2013) noticed high eccentricity and long orbital period of the system. Kjurkchieva et al. (2017) presented first photometric analysis of the system. No further analysis of the system has been provided so far. In this study, we present a comprehensive spectroscopic and photometric analysis of KIC 9028474. We briefly describe photometric and spectroscopic data in the next section. In Section 3, we give spectroscopic and photometric analyses, including analysis of Apache Point Observatory Galactic Evolution Experiment (APOGEE) spectra, radial velocity determination of the components, and simultaneous modeling of light and radial velocity curves. In the last section, we summarize and discuss our findings.

2. Data

2.1. Kepler Photometry

Photometric analysis of KIC 9028474 is based on long-cadence Kepler photometry. We extract each individual long-cadence flux from target pixel files (tpf).[2] A single exposure of Kepler photometry possesses an integration time of 6.02 s. These tpfs are created by summing 270 successive single exposures. Thus, each tpf practically corresponds to 1766 s of integration time and is labeled as a long-cadence measurement. We adopt PYTHON package LIGHTKURVE (Lightkurve Collaboration et al. 2018) for practical extraction of the data. After we extract the long-cadence data from tpf, we check the extracted data for inspecting and removing low-frequency trends, if any. If we determine a low-frequency trend, then we use *flatten* function of LIGHTKURVE software to remove the trend. Finally, we normalize the extracted data by *normalize* function defined in LIGHTKURVE software. We repeat these steps for each Kepler quarter, where every quarter has a time base of approximately 90 days, except the zeroth quarter, which is for spacecraft commissioning. We only exclude quarter 15 because for that quarter we are unable to reliably eliminate unwanted effects like low-frequency trends and sudden increases in brightness due to the thermal transient. We present the long-cadence light curve of KIC 9028474 in Figure 1.

2.2. Spectroscopic Data

Thanks to the APOGEE (Majewski et al. 2017) survey, considerable number of near-infrared APOGEE spectra of the

[1] http://keplerebs.villanova.edu/

[2] All the KEPLER data used in this paper can be found in MAST (STScI 2016).

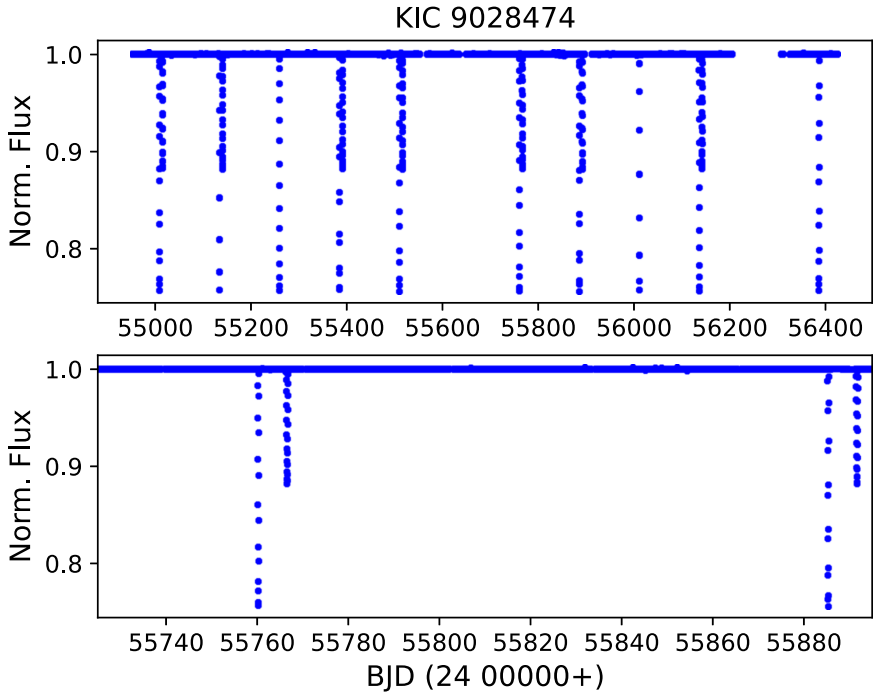

Figure 1. Long-cadence light curve (upper panel) of KIC 9028474. The very high eccentricity is easily noticeable from very short time interval between deep and shallow eclipses. The lower panel shows closer view of successive eclipses for a portion of the whole light curve.

system were obtained by a high resolution ($R = \lambda/\Delta\lambda \sim 22{,}500$) infrared spectrograph attached to the 2.5 m Sloan Foundation telescope (Gunn et al. 2006). Observed infrared spectra cover a wavelength range of 1.51–1.7 μm. Kounkel et al. (2021) published measured radial velocities for the both components of KIC 9028474 from 21 APOGEE spectra. However, although the radial velocity measurements of the primary component exist for each of the 21 spectra, no measurement is available for the secondary component among 15 of the 21 spectra. For that reason we obtain all available infrared spectra of our target system from the seventeenth data release of Sloan Digital Sky Survey (Jönsson et al. 2020; Abdurro'uf et al. 2022). We are able to find 22 APOGEE infrared spectra from the Science Archive Server[3].

3. Analysis

3.1. Radial Velocities

For radial velocity determination, we utilize the spectral broadening function (BF) method (Rucinski 1999, 2012). We compute a synthetic spectrum, which provides a closer match to the composite spectrum of the system and use the computed spectrum as a template for the application of the BF method. In practice, we make use of RAVESPAN code (Pilecki et al. 2013, 2017), which has a simple and useful graphical user interface and enables users to determine the radial velocity of target systems with three different methods, including the BF method. During the computation of BFs, we take into account all wavelength ranges of APOGEE spectra but only avoid distorted features (e.g., cosmic rays), which can not be fixed properly. We detect signals of both components for almost all APOGEE spectra recorded around the orbital quadratures of KIC 9028474. However, we do not detect a tertiary signal, which could be interpreted as a third light. We show broadening functions for two APOGEE spectra corresponding to orbital quadratures in Figure 2. We list measured radial velocities and their uncertainties in Table 1.

3.2. Effective Temperature and Metallicity

We use the advantage of high signal-to-noise ratio (S/N = 74) APOGEE spectrum of the system, which was recorded at BJD = 24,57264.8067, for estimating the effective temperatures of both components and overall metallicity of the system. In this spectrum, spectral lines of both components are clearly observed. We compute grids of synthetic spectrum for a given effective temperature, logarithmic surface gravity (log g), and metallicity. Computations are done by SPECTRUM code (Gray & Corbally 1994) by adopting MARCS model atmospheres (Gustafsson et al. 2008) and the third version of the Vienna atomic line database (Ryabchikova et al. 2015). For the practical computation of grids, we employ *iSpec* software (Blanco-Cuaresma et al. 2014), which includes several assorted radiative transfer codes, model atmospheres, line lists, and many useful features in a PYTHON environment. We compute synthetic spectrum grids between 4000 and 7000 K of effective temperature ($T_{\rm eff}$), 3.0–4.5 of log g, and −1.0–+0.25 of overall metallicity (in terms of [Fe/H]). The adopted steps for temperature, gravity and metallicity are 50 K, 0.1, and 0.25, respectively. During computations, we fix microturbulence velocity to 2 km s^{-1}, which is proper for solar-type main-sequence stars. We also fix log g values, which are computed from simultaneous light and radial velocity curve analysis (see next section). In preliminary analyses, we find no significant rotational broadening in spectral lines. This indicates slow rotational velocities for both components of KIC 9028474. Thus, we conclude that rotational broadening of the components is not measurable with the resolution of APOGEE spectra and we ignore the rotational broadening.

[3] https://data.sdss.org/sas/

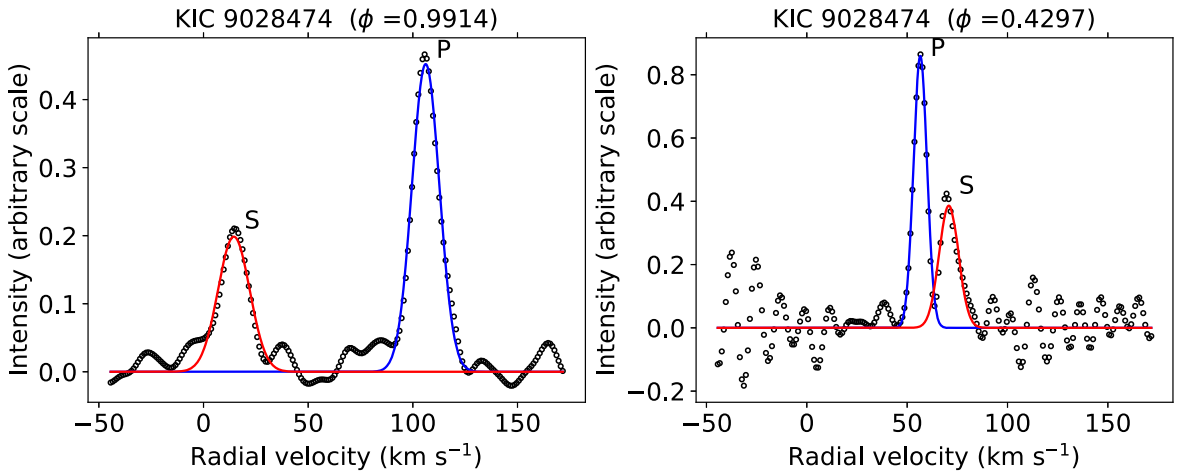

Figure 2. Broadening functions (small open circles) of two APOGEE spectra obtained in the close vicinity of the orbital quadratures. Gaussian fits for the primary (P) and the secondary (S) components are shown in continuous (blue and red) lines. The orbital phase (ϕ) of each observation is shown just above each panel.

Table 1
Measured Radial Velocities of the Components of KIC 9028474 and their Corresponding Uncertainties (σ) in km s^{-1}

BJD (2,400,000+)	RV_1 (km s^{-1})	σ_{RV_1} (km s^{-1})	RV_2 (km s^{-1})	σ_{RV_2} (km s^{-1})
56931.6929	60.3	0.2	72.0	0.3
57113.9630	53.6	0.3	75.5	0.4
57121.9476	54.8	0.6	73.7	1.2
57172.8198	59.6	0.2	66.4	0.2
57202.7111	54.9	0.7	72.7	1.5
57264.8067	106.6	0.5	15.0	1.0
57319.5705	56.8	0.7	72.8	1.4
57469.9853	53.8	0.4	75.5	0.8
57496.9484	54.9	0.6	73.3	1.3
57528.8813	69.9	0.3	57.5	1.1
57643.5968	85.4	0.5	38.8	1.1
57707.5436	54.8	0.5	73.8	1.0
57708.5492	54.4	0.7	73.6	1.3
57829.9755	54.6	0.6	73.1	1.2
58247.9514	54.7	0.9	71.4	2.2

Note. We note that we give all observing times as Barycentric Julian Date (BJD).

After grid computation ends, we choose two synthetic spectra (one for each component) among computed grids and shift each synthetic spectrum in the wavelength axis concerning the observed radial velocity of the corresponding component. Then, we combine shifted synthetic spectra by scaling each of them according to the square of the ratio of radii of the components and finally obtain the computed composite spectrum. Comparing the computed composite spectrum with the observed one, we calculate the χ^2 value for the current synthetic spectra pair. We repeat this procedure for all possibilities and compile χ^2 values of solutions. Evaluating the compiled χ^2 values, we search for a global minimum in parameter space for effective temperatures of the components and overall metallicity of the system. Finally, we obtain estimations for effective temperatures and metallicity. We use these estimated values in simultaneous light and radial velocity curve analysis and obtain physical parameters for the components of the system. After that, we update our adopted log g values in spectrum analysis with the computed log g values in simultaneous light and radial velocity curve analysis. Then, we repeat the procedure described above. We run this loop until we reach a self-consistent solution. Our analysis indicates that KIC 9028474 possesses solar metallicity, and the effective temperatures of the primary and the secondary components are 6050 K and 5850 K, respectively. These temperatures and adopted log g values indicate F9V and G1V spectral types according to the calibrations given in Gray (2005). Estimated uncertainties from χ^2 distribution are approximately 110 and 130 K for the primary and the secondary components, while it is 0.15 dex for [Fe/H]. In Figure 3, we show agreement between the observed and the best-matched composite synthetic spectra, together with residuals.

3.3. Simultaneous Analysis of Light and Radial Velocity Curves

Before we start simultaneous modeling, we first determine mideclipse times and construct an eclipse time variation (etv) diagram. In the beginning, we focus on the deeper eclipses in the long-cadence light curve and determine mideclipse times by fitting fourth-order polynomial to data points nearby of expected mideclipse. However, in the later stages of our analysis, we notice that the less massive and cooler component is eclipsed in the deeper eclipse in the Kepler light curve. Therefore, we adopt the midtime of the first observed shallow eclipse in the light curve as the reference epoch (T_0) and we consider the orbital period ($P_{\rm orb}$) reported in Kepler Eclipsing Binary catalog. Then, we compute the corresponding residual for each measured mideclipse time according to these light elements. We list measured mideclipse times and etv data in Table 2. Plotting the residuals against integer cycle number (E), we obtain Figure 4.

Inspecting Figure 4, we easily observe striking residuals around 56.15 days for the deep eclipses. This is a combined result of the very high eccentricity of the orbit, the very long orbital period, and the current position of the longitude of the periastron. Another notable feature observed in Figure 4 is that etv data of both eclipses exhibit variation in the same direction, but with a slight shift in cycle axis, which approximately corresponds to 300 days in time. Observed variation patterns of etv data may indicate the existence of a third body. However, the time base of the observations appears insufficient to catch the variation for a full period. Looking at the difference between residuals of shallow and deep eclipses, the apsidal

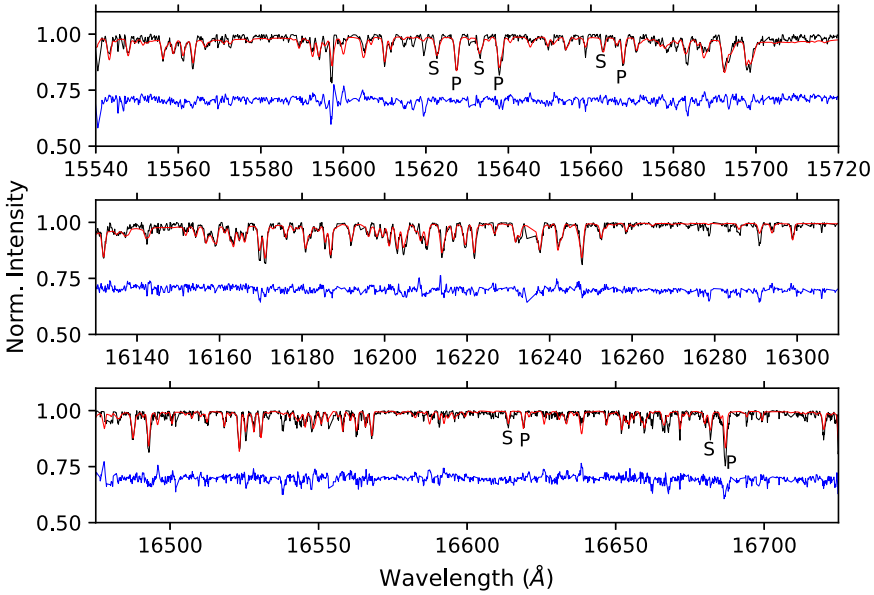

Figure 3. Observed APOGEE spectrum (black line) of KIC 9028474 at BJD = 2,457,264.8067 and the best-matched computed composite synthetic spectrum (red line). Three different parts of the APOGEE spectrum are shown in three panels. The blue line shows residuals from the best-matched computed composite synthetic spectrum and shifted upwards in the $-y$-axis for better viewing purposes. Clearly separated and unblended spectral lines of both components are marked as P and S for the primary and the secondary, respectively.

Table 2
Determined Mideclipse Times and their Corresponding Residuals

BJD (2,400,000+)	Error (days)	E	etv (days)
55016.9863	0.0017	0.0	0.0000000
55141.9228	0.0027	1.0	−0.0001180
55391.8048	0.0024	3.0	0.0084330
55516.7470	0.0018	4.0	0.0139930
55766.6278	0.0021	6.0	0.0214070
55891.5649	0.0026	7.0	0.0217890
56141.4311	0.0022	9.0	0.0146630
55010.6704	0.0022	−0.5	56.1525080
55135.6127	0.0027	0.5	56.1580670
55260.5563	0.0022	1.5	56.1650080
55385.4991	0.0027	2.5	56.1711230
55510.4401	0.0029	3.5	56.1753890
55760.3144	0.0027	5.5	56.1763140
55885.2476	0.0020	6.5	56.1728700
56010.1787	0.0031	7.5	56.1672750
56135.1083	0.0023	8.5	56.1602140
56384.9683	0.0029	10.5	56.1467730

Note. E shows integer orbital cycle number.

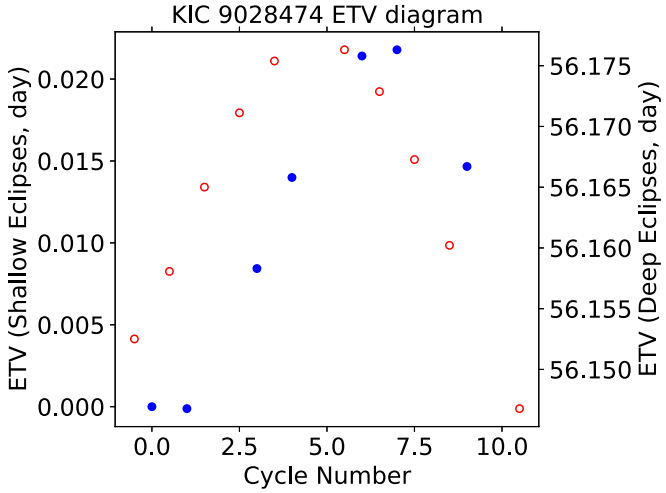

Figure 4. ETV diagram of KIC 9028474. Blue (filled) and red (open) circles denote etv of shallow and deep eclipses, respectively. We show etv of deep eclipses as the secondary axis for a better viewing purpose.

motion might be considered as another mechanism in progress in KIC 9028474. Due to the complex nature of the etv diagram, which suggests two separate mechanisms but includes a few data within a limited time range, we leave improvement of T_0 and $P_{\rm orb}$ to the simultaneous light and radial velocity analysis.

We carry out spectroscopic orbit and light curve modeling with the 2015 version of the Wilson–Devinney (WD) code (Wilson & Devinney 1971; Wilson & Van Hamme 2014) with the help of PYWD2015 software[4] (Güzel & Özdarcan 2020). PYWD2015 has a nice and practical graphical user interface that enables almost all features of the WD code (except subset solutions) to users. We adopt MODE 2 of the WD code, which is proper for detached eclipsing binaries and set coarse and fine surface grids of each component to 60. Our preliminary model runs indicate that a high number of surface grids are required for proper representation of sharp eclipses in the light curve. We implement the stellar atmosphere formulation and the simple reflection treatment for the computation of local emissions on both components. Estimated effective temperatures in the previous section indicate convective outer envelopes for both components, hence we set the gravity darkening (g_1, g_2) and the reflection coefficients (A_1, A_2) to 0.32 (Lucy 1967) and 0.5 (Ruciński 1969), respectively. Since we can not measure the rotation of stars from APOGEE spectra, we have no information about their synchronicity to the orbit, thus we implicitly assume synchronous rotation and set the rotation parameters of the components (F_1, F_2) to the unity. We assume linear limb-darkening law and let the WD code automatically compute the required coefficients (x_1, x_2) on

[4] https://github.com/Varnani/pywd2015-qt5

Table 3
Model Parameters and Corresponding Formal Errors (given in Parentheses for the Last Digits) of the Best-fitting Light Curve and Radial Velocity Curve Models

Parameter	Final Value
T_0 (BJD 2450000+)	5017.002(34)
$P_{\rm orb}$ (days)	124.93669(1)
e	0.82029(1)
ω (°)	340.4033(4)
$\Delta\phi$	0.2681(3)
V_γ (km s^{-1})	63.6(2)
a ($R_\odot$)	137(1)
q	0.88(2)
i (°)	88.441(2)
$T_{\rm eff1}$ (K)	6050 (110)
$T_{\rm eff2}$ (K)	5850 (130)
Ω_1	95.1(1)
Ω_2	113.9(3)
$L_1/L_{\rm tot}$	0.683(1)
x_1	0.526
x_2	0.549
$\langle r_1\rangle$	0.01109(1)
$\langle r_2\rangle$	0.00811(3)
Rms ($\times10^{-3}$)	0.245

Note. Note that the uncertainties of $T_{\rm eff1}$ and $T_{\rm eff2}$ are adopted from the analysis of the APOGEE spectrum in previous sections. Mean fractional radii are shown with $\langle r_1\rangle$ and $\langle r_2\rangle$ for the primary and the secondary components, respectively.

the fly from tables provided by van Hamme (1993) during differential corrections (DC) runs. Considering our effective temperature estimations, we set $T_{\rm eff1}$ to 6050 K and keep it fixed during the whole analysis. We load the whole long-cadence light curve data (57,496 measurements in total) and the radial velocity data to PYWD2015 and set the weight of each individual data point to one. For the light curve data, we set light level-dependent weighting with respect to the inverse of the square root of the light level.

After we establish our model assumptions and set fixed parameters, we start to make trial models for the observed light and radial velocity data by adjusting the following parameters: the epoch (T_0), the orbital period (P), the semimajor axis (a), the mass ratio ($q = M_2/M_1$) in terms of secondary over primary star, the center-of-mass velocity of the system (V_γ), the eccentricity of the orbit (e), the longitude of the periastron (ω), the phase shift ($\Delta\phi$), the inclination of the orbital plane (i), the effective temperature of the secondary component ($T_{\rm eff2}$), the dimensionless surface potentials of the components (Ω_1, Ω_2), and the luminosity of the primary component (L_1). When we get a reasonably good match between the trial models and the observations, we start DC runs and try to improve all the parameters summarized above simultaneously. In the analysis, we also set third light (ℓ_3) as adjustable parameters and check whether there is a significant contribution of ℓ_3 to the models. We carried out differential corrections runs until corrections for all parameters become smaller than their corresponding formal uncertainties reported by the WD code. We observe the ℓ_3 parameter mostly jiggles around zero level with very small positive or negative values in DC runs and does not converge to a reasonable value. Hence we set $\ell_3 = 0$ and continue DC runs without third light contribution. Finally, DC runs move adjustable model parameters to a global minimum in parameter space. The final values of the adjustable parameters, which provide the best match for the observed light and radial velocity curves, are listed in Table 3. In Figure 5, we present a visual illustration of the observations and the best-matched models. We note that there is a clear regular scatter around eclipse phases for both deep and shallow minima, which indicates the light time travel effect and suggests a tertiary component in the system. Besides this scatter, we do not observe any significant brightness variability at out-of-eclipse parts of the light curves. Considering the information given in Table 3, we compute the fundamental parameters of each component and list them in Table 4. We estimate uncertainties of the fundamental properties by perturbing the parameters in Table 3 with their corresponding formal errors.

In addition to the fundamental parameters, we also inspect the distance of the system by considering measured *UBV* magnitudes and colors of the system by Everett et al. (2012). Our preliminary inspections on the *UBV* color–color diagram do not indicate any significant interstellar reddening, thus we omit color excess and interstellar extinction in the distance calculation. Adopting bolometric correction calibrations of Girardi et al. (2002), we compute distance for each of *U*, *B,* and *V* passbands. The average of the three distances is $d = 746 \pm 35$ pc, which we consider as the final distance of the system. This value is remarkably higher than 629 ± 4 pc of distance estimated by GAIA parallaxes (Gaia Collaboration et al. 2016, 2023). This picture leads us to look for a possible interstellar reddening, which we can not detect from *UBV* colors. Dust maps of Schlafly et al. (2014) suggests $E(B-V) = 0\overset{\rm m}{.}167 \pm 0\overset{\rm m}{.}016$ for the precise galactic coordinates of KIC 9028474. Recomputing the distance with this reddening amount, we find $d = 543 \pm 30$ pc, which is still different but this time closer than the GAIA distance. However, our latest and final distance value is in agreement within 1σ level with the distance estimation of Leung & Bovy (2019; 459 ± 74 pc).

3.4. Evolutionary Status

In Figure 6, we show the positions of both components of KIC 9028474 on $\log T_{\rm eff} - \log L/L_\odot$ plane. Evolutionary tracks and isochrones in the figure are from Bressan et al. (2012). Among different helium and heavy element abundances, the closest match with the masses of the components is obtained with $Y = 0.284$ and $Z = 0.02$ model, which approximately corresponds to [Fe/H] = 0.12. This indicates a slightly large overall metallicity for the system compared to the solar value. However, considering the estimated uncertainty (±0.15 dex) of the overall metallicity in previous sections, we conclude that the system possesses solar metallicity. Evaluating isochrones, which provide close matches to the positions of the components, we estimate the age of KIC 9028474 as 5.2 ± 0.8 Gyr. It appears that the primary component is very close to the end of the core hydrogen burning phase and is about to leave the main sequence.

4. Summary and Discussion

Combined analysis of infrared APOGEE spectra and Kepler photometry shows that KIC 9028474 is a very long-period solar-type eclipsing binary composed of F9V+G1V components on a highly eccentric orbit. The primary component in the system is close to leaving the main sequence and indicating 5.2 ± 0.8 Gyr age for the system. Adopting moderate

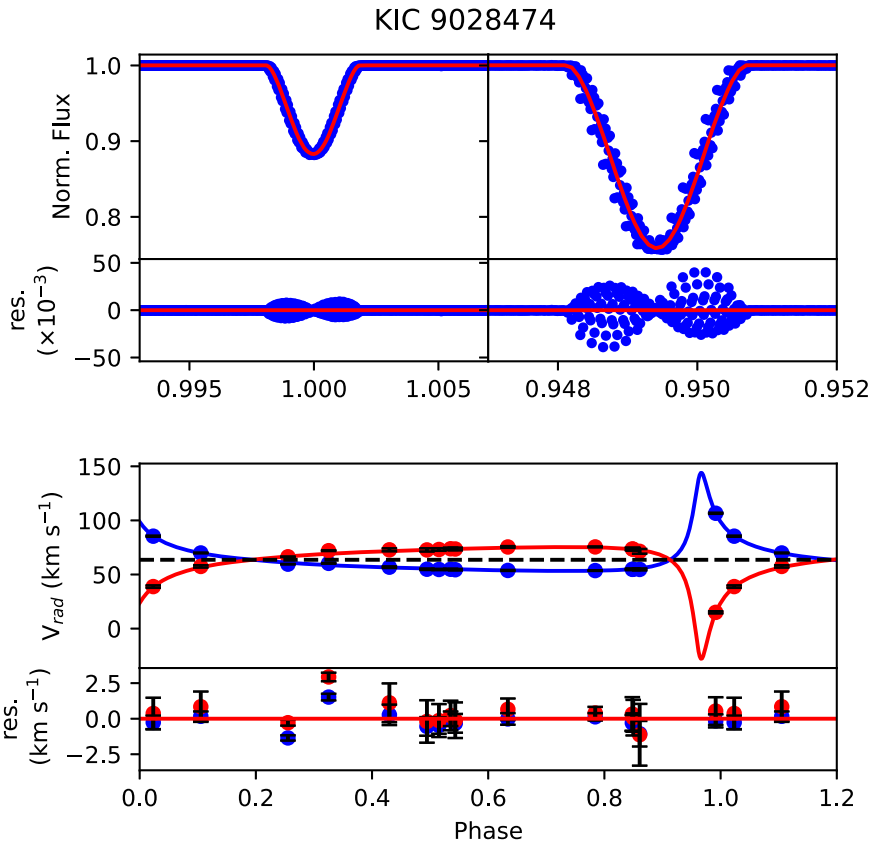

Figure 5. Representations of the phase-folded light curve (upper panel) and radial velocity curve (lower panel). The best-matched light curve model is shown with the red curve. Regarding radial velocities, blue and red colors are for the primary and the secondary components, respectively. Observational uncertainties are often smaller than the size of the circles in the lower panel. Phase folding is done with respect to the T_0 and $P_{\rm orb}$ given in Table 3.

Table 4
Fundamental Properties of the Components of KIC 9028474

Parameter	Value
M_1 ($M_\odot$)	1.18(4)
M_2 ($M_\odot$)	1.04(3)
R_1 ($R_\odot$)	1.52(2)
R_2 ($R_\odot$)	1.11(1)
log g_1 (cgs)	4.146(6)
log g_2 (cgs)	4.362(7)
log L_1 ($L_\odot$)	0.45(3)
log L_2 ($L_\odot$)	0.12(4)

interstellar reddening of $E(B-V) = 0\overset{\rm m}{.}167$, the distance of the system is computed as $d = 543 \pm 30$ pc.

ETV diagram of the system exhibits a striking difference (≈56 days) between the residuals of the deep and the shallow eclipses. Such a large difference is the combined result of the long period, high eccentricity, and current position of the longitude of the periastron. In such a system, observing apsidal motion would not be a surprise. However, we only have seven and ten data points for the shallow and the deep eclipses, respectively. These data points cover only ten successive orbital cycles. We believe that a reliable inspection of a possible apsidal motion is not likely in this case. Nevertheless, we estimate the rate of change of the argument of periastron due to the contributions of relativistic ($\dot{\omega}_{\rm rel}$) and tidal ($\dot{\omega}_{\rm tidal}$) effects. Following equations of Gimenez (1985) and using theoretical tidal evolution constants (only for the first order)

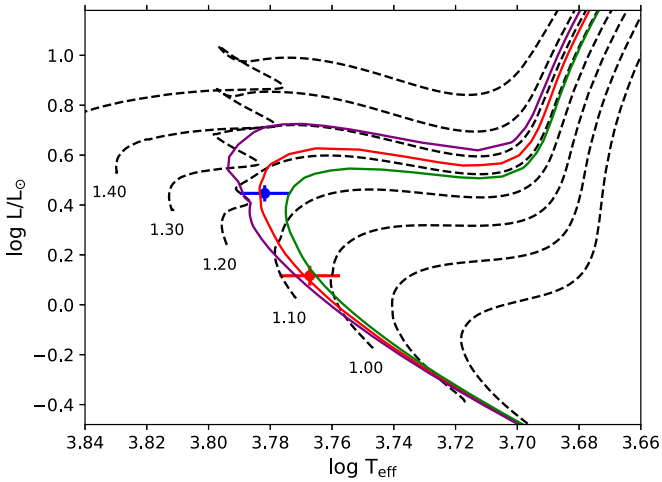

Figure 6. Positions of the components in $\log T_{\rm eff} - \log L/L_\odot$ plane. Three different isochrones for log age 9.5, 9.7, and 9.8 are also plotted with continuous curves. Dashed curves show evolutionary tracks for different masses. Each track is labeled with its corresponding mass in the solar unit.

from Claret (2019), we find $\dot{\omega}_{\rm rel} = 0\overset{\circ}{.}000113\,{\rm cycle}^{-1}$ and $\dot{\omega}_{\rm tidal} = 10^{-8\circ}\,{\rm cycle}^{-1}$. Since we do not have a reliable observed $\dot{\omega}$ value, we are unable to make a comparison with the computed theoretical values above, but we give these estimations as speculations to be tested with further observations.

On the other hand, the ETV diagram and the residuals from the best-matched light curve model suggest the existence of a third body that is physically connected to the system. Such a

third body may excite the eccentricity of the orbit of the eclipsing pair due to the Kozai–Lidov cycles. In other words, a possible third body in the system might be partly responsible for the very high eccentricity of the orbit. However, we do not detect any signal for a tertiary component in the light curve analysis and the spectral broadening functions. Future photometric observations become important to obtain further eclipses of the system in order to reveal the real nature of the signals observed in etv diagram of KIC 9028474.

We do not observe any rotational broadening for spectral lines in the APOGEE spectra of the system and there is no out-of-eclipse brightness variation in the residual light curve, hence we can not obtain direct or indirect information about the rotation of the components. As a result, we implicitly assume synchronous rotation to the orbit for the components. Under this assumption, we compute equatorial rotational velocity ($v_{\rm eq}$) of each component as $v_{\rm eq1} = 0.6\ {\rm km\ s^{-1}}$ and $v_{\rm eq2} = 0.4\ {\rm km\ s^{-1}}$. These findings indicate that the rotational velocities of both components are very low and they do not possess magnetic cool surface spots, which are common properties of solar-type stars exhibiting magnetic activity. This is not an unexpected situation for such a long-period system with very slowly rotating components since noticeable magnetic activity requires significantly higher rotational velocity.

Physical properties of the components suggest 10^{12} and 10^{16} years for circularization and synchronization timescales according to the theoretical predictions of Zahn (1977). On the other hand, Tassoul (1988) suggests that the hydrodynamical process should be more dominant compared to the dynamical and equilibrium tides in wide binaries. Following his equations, we find 10^{13} yr for the circularization timescale, which is ten times longer than Zahn's prediction. Considering the estimated age of the system, the current eccentricity of the system is in agreement with Zahn's and Tassoul's predictions. It appears that both components will evolve and end their life much before the circularization of the orbit happens. Regarding the synchronicity of the components, we are unable to arrive at any meaningful conclusion because we have no precise information on the rotational periods of the components. However, according to Zahn's theory, synchronization of the components to the orbit appears unlikely during the whole evolution (including post-main-sequence phases) of the system.

As mentioned above, detecting further eclipse of the system is critical to track the etv signals of KIC 9028474 and investigate the apsidal motion and the third body possibilities. Very-high-resolution ($R = \lambda/\Delta\lambda > 100{,}000$) spectroscopic observations might help to detect rotational velocities of the components if one or both have a supersynchronous rotation and possess rotational velocities of a few ${\rm km\ s^{-1}}$. Otherwise, high-precision space photometry is left as the only key to extract information on the rotation of components from the rotational modulation of cool stellar spots. This also can not be guaranteed in the case of KIC 9028474 because a long orbital period (i.e., low rotational velocities of the components) possibly causes very-low-level magnetic activity. This may prevent us from photometric detection of the rotational modulation, which is the sign of cool stellar surface spots that are photometric proxies of magnetic activity.

Acknowledgments

We thank the anonymous referee for taking the time and effort to review the manuscript and appreciate the detailed comments and criticisms that improve the quality of the manuscript. This research made use of NASA's Astrophysics Data System Bibliographic Services and SIMBAD database, operated at CDS, Strasbourg, France. This paper includes data collected by the Kepler mission. Funding for the Kepler mission is provided by the NASA Science Mission Directorate.

Facility: 2.5 m Sloan Digital Sky Survey (SDSS) Telescope at Apache Point Observatory (APO).

Software: lightkurve (Lightkurve Collaboration et al. 2018), numpy (Harris et al. 2020), scipy (Virtanen et al. 2020), matplotlib (Hunter 2007).

ORCID iDs

Orkun Özdarcan https://orcid.org/0000-0003-4820-3950

References

Abdurro'uf, Accetta, K., Aerts, C., et al. 2022, ApJS, 259, 35
Andersen, J. 1991, A&ARv, 3, 91
Blanco-Cuaresma, S., Soubiran, C., Heiter, U., & Jofré, P. 2014, A&A, 569, A111
Bressan, A., Marigo, P., Girardi, L., et al. 2012, MNRAS, 427, 127
Claret, A. 2019, A&A, 628, A29
Dong, S., Katz, B., & Socrates, A. 2013, ApJL, 763, L2
Everett, M. E., Howell, S. B., & Kinemuchi, K. 2012, PASP, 124, 316
Gaia Collaboration, Prusti, T., de Bruijne, J. H. J., et al. 2016, A&A, 595, A1
Gaia Collaboration, Vallenari, A., Brown, A. G. A., et al. 2023, A&A, 674, A1
Gimenez, A. 1985, ApJ, 297, 405
Girardi, L., Bertelli, G., Bressan, A., et al. 2002, A&A, 391, 195
Gray, D. F. 2005, The Observation and Analysis of Stellar Photospheres (2nd ed.; Cambridge: Cambridge Univ. Press)
Gray, R. O., & Corbally, C. J. 1994, AJ, 107, 742
Gunn, J. E., Siegmund, W. A., Mannery, E. J., et al. 2006, AJ, 131, 2332
Gustafsson, B., Edvardsson, B., Eriksson, K., et al. 2008, A&A, 486, 951
Güzel, O., & Özdarcan, O. 2020, CoSka, 50, 535
Harris, C. R., Millman, K. J., van der Walt, S. J., et al. 2020, Natur, 585, 357
Hunter, J. D. 2007, CSE, 9, 90
Jönsson, H., Holtzman, J. A., Allende Prieto, C., et al. 2020, AJ, 160, 120
Kjurkchieva, D., Vasileva, D., & Atanasova, T. 2017, AJ, 154, 105
Kounkel, M., Covey, K. R., Stassun, K. G., et al. 2021, AJ, 162, 184
Leung, H. W., & Bovy, J. 2019, MNRAS, 489, 2079
Lightkurve Collaboration, Cardoso, J. V. d. M., Hedges, C., et al., 2018 Lightkurve: Kepler and TESS Time Series Analysis in Python, Astrophysics Source Code Library, ascl:1812.013
Lucy, L. B. 1967, ZAp, 65, 89
Majewski, S. R., Schiavon, R. P., Frinchaboy, P. M., et al. 2017, AJ, 154, 94
Pilecki, B., Gieren, W., Smolec, R., et al. 2017, ApJ, 842, 110
Pilecki, B., Graczyk, D., Pietrzyński, G., et al. 2013, MNRAS, 436, 953
Prša, A., Batalha, N., Slawson, R. W., et al. 2011, AJ, 141, 83
Rucinski, S. 1999, TJPh, 23, 271
Ruciński, S. M. 1969, AcA, 19, 245
Rucinski, S. M. 2012, in IAU Symp. 282, From Interacting Binaries to Exoplanets: Essential Modeling Tools, ed. M. T. Richards & I. Hubeny (Cambridge: Cambridge Univ. Press), 365
Ryabchikova, T., Piskunov, N., Kurucz, R. L., et al. 2015, PhyS, 90, 054005
Schlafly, E. F., Green, G., Finkbeiner, D. P., et al. 2014, ApJ, 789, 15
Slawson, R. W., Prša, A., Welsh, W. F., et al. 2011, AJ, 142, 160
STScI 2016, Kepler LC, Q0-Q17, STScI/MAST, doi:10.17909/T9488N
Tassoul, J.-L. 1987, ApJ, 322, 856
Tassoul, J.-L. 1988, ApJL, 324, L71
van Hamme, W. 1993, AJ, 106, 2096
Virtanen, P., Gommers, R., Oliphant, T. E., et al. 2020, NatMe, 17, 261
Wilson, R. E., & Devinney, E. J. 1971, ApJ, 166, 605
Wilson, R. E., & Van Hamme, W. 2014, ApJ, 780, 151
Zahn, J. P. 1975, A&A, 41, 329
Zahn, J. P. 1977, A&A, 57, 383